Article

Photo(electro)catalyst of Flower-Like Cobalt Oxide Co-Doped g-C$_3$N$_4$: Degradation of Methylene Blue under Visible Light Illumination

Qiuhua Li [1,2] and Qunhui Wang [1,*]

1   School of Energy and Environmental Engineering, University of Science and Technology Beijing, Beijing 100083, China; wyuchemlqh@126.com
2   School of Biotechnology and Health Sciences, Wuyi University, Jiangmen 529020, China
*   Correspondence: wangqh59@163.com; Tel.: +18-60-024-8303

Abstract: This work reported on the solid state synthesis of the flower-like Co(OH)$_2$/g-C$_3$N$_4$ nanocomposite, using a modified hydrothermal method, for the degradation of MB, an organic pollutant. These nanomaterials were characterized for structure, surface morphology and composition using XRD, SEM and XPS, respectively. The photocatalytic activities of the as-prepared materials loaded on FTO glass substrates were evaluated for their degradation of methylene blue (MB) under visible irradiation and constant voltage. The promoting effect of Fw-Co(OH)$_2$ on g-C$_3$N$_4$ was investigated under the influence of introduced various Co(OH)$_2$ amounts. The fabricated composite catalyst showed significantly improved catalytic performance compared to pristine g-C$_3$N$_4$. Degradation by 25% Fw-Co(OH)$_2$/g-C$_3$N$_4$ can achieve about a 100% ratio within 180 min under visible light in a three-electrode system. Moreover, Fw-Co(OH)$_2$/g-C$_3$N$_4$ was easily regenerated and reused, and still possessed good degradation ability. These results suggest that Fw-Co(OH)$_2$/g-C$_3$N$_4$ could be promising for application as a low-cost and high-efficiency catalyst for wastewater treatment and organic pollutant degradation.

Keywords: Co(OH)$_2$; g-C$_3$N$_4$; methylene blue dyes; photo(electro)catalyst

1. Introduction

Water pollution escape from different dye industries including paper, leather, textiles and plastics, has become a critical problem in the world [1] since the dyes used, even at low concentrations, are toxic and threatening to the aquatic system and human health [2]. Various techniques, such as adsorption, membrane processes, electrochemical treatment, photo decomposition and biological methods, have been developed to remove dyes from wastewater [3,4]. Among these methods, from carbon nanoflakes for selective adsorption of water-soluble cationic dyes (MB), to anionic dyes [5], nanofibrous membranes can be used to enhance ion exchange properties. They are promising candidates for the treatment of dye-laden wastewater [6]. Cellulose/alginate monolithic hydrogel is a highly effective adsorbent for methylene blue (MB) removal [7], and photocatalytic degradation based on semiconductors has attracted increasing attention. This is an approach which leads to the generation of free radicals towards water pollution treatment. Eco-friendly and stable photocatalysts, such as TiO$_2$, Fe$_2$O$_3$, CdS and ZnO, have proven to be suitable photocatalysts for the removal of organic water pollutants [8–10]. Noble metal catalysts have low ignition temperatures and high catalytic activity, but they are expensive and easy to deactivate, and thus cannot be widely used in business. Non-metallic catalysts are low in cost, with sufficient activity and excellent stability; recently, the metal-free g-C$_3$N$_4$ photocatalysts have attracted increasing attention [11].

Compared with other wide band-gap semiconductor materials, metal-free g-C$_3$N$_4$ photocatalysts have a unique band structure which can enable g-C$_3$N$_4$ to absorb more

visible light. Moreover, such catalysts have better thermal and chemical stability in addition to remarkable electronic properties. Hence, g-C$_3$N$_4$ semiconductors have been used in various applications, for example, in the purification of contaminated water, CO$_2$ reduction, hydrogen evolution, energy storage and in humidity sensors [12]. However, the photocatalytic activity of g-C$_3$N$_4$ is still low. In order to solve the problem, many methods, including synthesis techniques, nanostructure design and electronic structure modulation have been proposed, in order to improve the photocatalytic performance of g-C$_3$N$_4$ [13–15]. Among them, deposition of efficient alternative semiconductors onto g-C$_3$N$_4$ has proven to be a feasible and effective measure to enhance its photocatalytic activity and efficiency. Nanocomposites with heterojunctions can effectively enhance the separation of electron-hole pairs and improve charge-separation efficiency, resulting in improved photocatalytic performance [16]. Liu et al. [17] prepared g-C$_3$N$_4$ nanosheets coupled with co-catalyst platinum (Pt), and used them for water splitting. Patnaik et al. [18] summarized the recent significant advances in designing Ag-modified g-C$_3$N$_4$-based nanocomposites in order to promote their photocatalytic activity.

Cobalt hydroxide (Co(OH)$_2$) is attracting increasing attention due to its low cost, earth abundance and unique redox property. Co(OH)$_2$ has two types of crystal structure, the α and β phase. Compared to β phase, α phase has a layered structure with relatively larger interlayer spacing, which could enhance the diffusion of ions and become beneficial for electrochemical applications. Its relatively open structure enables rapid diffusion of reactants or products and rapid proton-coupled electron transfer, which make the catalytic active sites easily accessible; this results in high catalytic activity [19–21]. Recently, it has been reported that layers of flower-like Co(OH)$_2$ assembled with numerous of nanosheets possess excellent structural stability, in addition to optical, electrochemical, electromagnetic adsorptional properties and high selectivities, leading to great potential in for use in water oxidation, supercapacitors, and microwave adsorption materials [22–24]. However, to the best of our knowledge, no published papers exist about transition-metal hydroxides.

In order to enhance the photo(electro)catalytic degradation effect, we are going to begin research on the synthesis of Co(OH)$_2$-decorated g-C$_3$N$_4$ heterojunction composite (Fw-Co(OH)$_2$/g-C$_3$N$_4$), and also plan to develop different techniques to study the ability of the synthetic material (Fw-Co(OH)$_2$/g-C$_3$N$_4$) to remove methylene blue (MB) from waste water via its photo(electro)catalytic action.

2. Materials and Methods

2.1. Materials

Cobalt(II) nitrate hexahydrate (≥99.0%), Cobalt(II) acetate tetrahydrate (≥99.5%), urea (≥99%), Methanol (≥99.5%), Polyvinylpyrrolidone (PVP, ≥98.0%, Shanghai Maclean Co., LTD, Shanghai, China) and 5,5-dimethyl-1-pyrroline-N-oxide (DMPO; ≥97.0%). All the other chemicals were purchased from Guangzhou Chemical Reagent Co., LTD, Guangzhou, China. All chemicals are analytical grade, and used as received without further purification.

2.2. Preparation of Film Electrodes

The g-C$_3$N$_4$ semiconductor was obtained by thermal treatment. In a conventional process, 5 g of urea as precursor was put into a crucible and calcined at 550 °C for 2 h in air. Flower-like Co(OH)$_2$ was synthesized using a modified hydrothermal method. First, 0.498 g of Co(CH$_3$COO)$_2$·4H$_2$O, 0.24 g of urea and 0.5 g of polyvinylpyrrolidone (PVP, K30) were precisely added and dissolved in 40 mL of methanol. After 20 min of ultrasonication, the aqueous solutions were transferred into a 120-milliliter Teflon-steeled autoclave and heated at 200 °C for 6 h in an oven. The pink precipitate was separated by centrifugation, repeatedly rinsed with water and ethanol several times, and then dried at 60 °C under vacuum; the final product was Fw-Co(OH)$_2$. The synthesized Co(OH)$_2$ particles were dispersed in 5 mL of ethanol under ultrasonic treatment for at least 20 min until it was mixed uniformly. Carbon nitride powders were dispersed and sonicated in 20 mL of ethanol for another 15 min, then the above Co(OH)$_2$ suspension was added to the mixture.

The mixture was dried in an oil bath at 80 °C overnight, in order to remove ethanol. Then, the uniform powders were annealed at 120 °C in a muffle furnace for 2 h, obtaining X% Fw-Co(OH)$_2$/g-C$_3$N$_4$ composites. X% is the weight ratio of Fw-Co(OH)$_2$. The materials of synthesis in addition to the degradation process are shown in Figure 1.
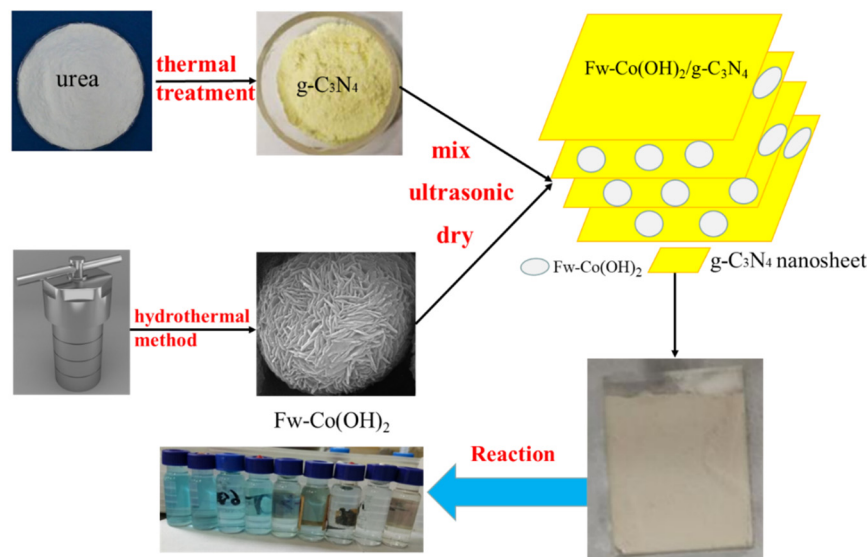

Figure 1. Schematic diagram of the synthesis process.

2.3. Characterization

X-ray diffraction (XRD) patterns were recorded on an X-ray diffractometer (Bruker, Bremen, Germany) with Cu-Kα radiation (λ = 1.5406 Å) over a 2θ angle range of 10–80°. X-ray photoelectron spectroscopy (XPS) were collected on a K-alpha X-ray photoelectron spectrometer (Thermo ESCALAB 250Xi, Carlsbad, CA, USA) with monochromatic Al Kα (hv = 1486.6 eV) from an X-ray source operating at 15 kV and 10 mA. All binding energies were referenced to the C 1s peak at 284.6 eV. The morphology of the photocatalysts were investigated via a scanning electron microscope (SEM, FEI Quanta 400 FEG), which was equipped with energy dispersive spectroscopy (EDS). High-resolution transmission electron microscopy (HRTEM) images were measured using a FEI Tecnai G2 F20 (HRTEM, FEI, Hillsboro, OR, USA), with an accelerating voltage of 200 kV. UV–visible diffuse reflectance spectra (UV–vis DRS) of the samples were measured on a UV–visible spectrophotometer (UV-2600, SHIMADZU, Kyoto, Japan) over the range of 200–800 nm using BaSO$_4$ as a reference. The binding energy was calibrated with reference to the C1 s peak at 284.8 eV.

2.4. Photoelectrochemical Measurements

Photocurrents were measured by an electrochemical analyzer (PARSTAT-4000, Oak Ridge, TN, USA) in a standard three-electrode system, using a Pt sheet (2 × 2 cm^2) as the counter electrode and saturated calomel electrode (SCE) as the reference electrode. Each conductive F-doped tin oxide (FTO) glass (effective area 2 × 2 cm^2) was cleaned using sonication in ethanol for 30 min, dried at 80 °C and then coated with a thin layer of Fw-Co(OH)$_2$/g-C$_3$N$_4$ catalyst as the substrate. The catalyst layer was prepared with 8 mg as-prepared sample powder (Fw-Co(OH)$_2$/g-C$_3$N$_4$) in a solution of 50 µL of Nafion (5 wt%) and 25 mL of ethyl alcohol. The catalyst suspensions were transferred to the FTO glasses using a pipette and then dried at 60 °C. The loading of catalyst on the electrode was ≈2 mg/cm^2. A 300-Watt xenon arc lamp (PLS-SXE300, Bofeilai Technology Co., Ltd., Beijing, China) with an excitation wavelength of 420 nm was used as the visible light source. A 0.1 M Na$_2$SO$_4$ aqueous solution was used as the electrolyte. For photocurrent measurement (I–t curves), the aforementioned 300-Watt Xe lamp was equipped with a 420 nm cut-off filter as the light source.

2.5. Photo(electro)catalytic Degradation

The catalytic activities of samples (prepared Fw-Co(OH)$_2$/g-C$_3$N$_4$ catalyst loaded onto FTO glass substrates) were evaluated by photo(electro)catalytic decomposition of MB. The materials of the degradation process are shown in Figure 1. The photocatalysis test was carried out with a 100-milliliter solution of MB (0.1 mol/L) under visible irradiation and constant voltage. The light was obtained from a 300-Watt Xe lamp with a 420 nm cutoff filter. The distance between the samples and lamp was 10 cm, with a constant light intensity of 200 W. The constant voltage was provided by a voltage source of 3 V. Prior to irradiation, the fabricated 2.0 × 2.0 cm^2 samples were immersed in the MB (100 mL, 0.1 M) solution that reacted with the catalyst electrode for 0.5 h in the dark at room temperature, in order to establish an adsorption/desorption equilibrium. The concentrations of MB in the sampled solutions were monitored by a UV–visible spectrophotometer (UV-2600, SHIMADZU) at its characteristic wavelength (k = 665 nm). The ratio of MB concentrations C/C$_0$ could be calculated using C/C$_0$ = A/A$_0$, where C$_0$ and C are the concentrations of MB solution at irradiation time 0 and t, respectively, and the respective A$_0$ and A are the corresponding absorbance values at 665 nm. In the durability testing, three successive cycles were performed. After each cycle (V = 3 V, LI = 200 W), the photocatalysts were washed with ethanol and deionized water carefully, and then dried at 60 °C for 12 h. Then, the used photocatalysts were inserted into fresh 0.1 mol/L pollutant solution in order to carry out the next photoelectrochemical activity testing.

This paper evaluated MB degradation efficiency as a result of an applied electric field and photocatalyst; different parameters combinations were applied: (i) four different voltage values at the same light intensity (200 W) were specified: 0 V, 1 V, 2 V and 3 V, and (ii) four different light intensities at the same voltage (3 V) were employed: 0 W, 50 W, 100 W and 200 W. The light intensity was measured by the PL-MW2000.

3. Results

3.1. Characterization of Fw-Co(OH)$_2$/g-C$_3$N$_4$

It can be seen clearly that the (100) and (002) peaks of g-C$_3$N$_4$ are at 13.1° and 27.4°, respectively [25]. The XRD pattern of cobalt hydroxide display diffraction peaks at 2θ values of 10.5, 21.3, 33.2, 37.1, 57.9 and 59.4° (Figure 2), which could be indexed to (003), (006), (012), (015), (110) and (013), respectively; these reflect a hydrotalcite-like α-Co(OH)$_2$ structure rather than the standard β-Co(OH)$_2$ with a broad diffraction peak between about 20° and 30° [26,27]. The maximal diffraction peak exhibited two series of diffraction peaks, which can be indexed to the α-Co(OH)$_2$ and g-C$_3$N$_4$, respectively. The hydrolysis reaction of urea with crystallized water in cobaltous acetate generates OH$^-$ anions, which reacted with Co^{2+} to form Co(OH)$_2$.
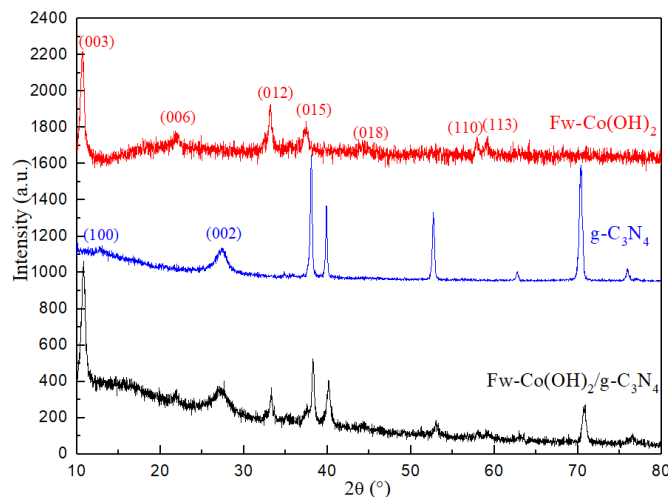

Figure 2. The XRD patterns of Fw-Co(OH)$_2$, g-C$_3$N$_4$ and Fw-Co(OH)$_2$/g-C$_3$N$_4$ composites.

Figure 3a shows that the SEM images of the g-C_3N_4 nanosheets, which exhibit a layered morphology and a sheet-like structure. From the SEM images of Fw-Co(OH)$_2$ in Figure 3b,c, it can be intuitively observed that the morphology of the samples are nanospheres around 2 μm in diameter. Detailed observations show that these 3D flower-like architectures are constructed by intertwined two-dimensional (2D) nanosheets with thicknesses of around 20 nm. According to the literature, with the assistance of PVP, the hydroxides are assembled into rod and then flake precipitates which stack and form flower-like architectures. As seen in Figure 3d–f, an SEM image of the boundary of the Fw-Co(OH)$_2$ nanoparticles is displayed in g-C_3N_4, indicating the formation of Fw-Co(OH)$_2$/g-C_3N_4 heterostructures in as-prepared 25% Fw-Co(OH)$_2$/g-C_3N_4 samples (the weight ratio of Fw-Co(OH)$_2$ and Fw-Co(OH)$_2$ is 1:3) [11]. The combined nanosheet structure of g-C_3N_4 and Fw-Co(OH)$_2$ not only provides abundant adsorption sites for the MB molecules, but also greatly shortens the transport distance of photogenerated charge carriers. TEM image shown in Figure 3g,h, was used to further explore the detailed structure of the g-C_3N_4 and Fw-Co(OH)$_2$/g-C_3N_4 sample, and indicated the formation of Fw-Co(OH)$_2$/g-C_3N_4 heterostructures in as-prepared 25% Fw-Co(OH)$_2$/g-C_3N_4 samples. Elemental mapping of the Fw-Co(OH)$_2$/g-C_3N_4 microparticles recorded using energy dispersive spectroscopy are shown in Figure 3j–n), where red, green, purple and black refer to C, N, Co and O elements, respectively, indicating that the cobalt hydroxide compound was distributed over the surface of the g-C_3N_4 base material. EDX results, as shown in Figure 3i, prove that the weight ratios of Co and C in both flower-like 25% Fw-Co(OH)$_2$/g-C_3N_4 nanostructures are both 1.1:1, which are consistent with the preparation conditions.

X-ray photoelectron spectroscopy analysis was employed to reveal the surface chemical composition and the detailed electronic states of different elements in g-C_3N_4 and in Fw-Co (OH)$_2$/g-C_3N_4 composites. The XPS survey spectra (Figure 4a) suggests that the Fw-Co(OH)$_2$/g-C_3N_4 was primarily composed of C, N, O and Co, further confirming the co-existence of g-C_3N_4 and Fw-Co (OH)$_2$/g-C_3N_4 in the composite. The C1 s spectra (Figure 4b) showed two deconvoluted peaks at 288.6 eV and 284.8 eV, ascribed to the signals of sp2-bonded carbon (N-C=N) and standard reference carbon, which is usually observed in the XPS spectra of carbon nitrides [28]. In addition, the N 1s spectrum in Figure 4c can be deconvoluted into four peaks located at 398.9 eV, 399.6 eV, 400.9 eV and 405 eV, which can be assigned to C=N-C, (C)$_3$-N, quaternary N bonded to three carbon atoms in the aromatic cycles, and the π citations, respectively [17,29]. In conjunction with the above results, except for the peaks' intensities, the bonding characteristics of C1 s and N1 s showed no apparent change between g-C_3N_4 and Fw-Co (OH)$_2$/g-C_3N_4. The existence of Co (OH)$_2$ can be further certified by high resolution XPS analysis of Co 2p. In Figure 4d, the high XPS resolution of Co 2p can be deconvoluted into two pairs of individual peaks at 783.0 eV and 798.3 eV, respectively, which were identified as the major binding energies of Co^{2+} in Co (OH)$_2$ [20].

3.2. Optical Studies

The UV–vis diffuse reflectance spectra of as-prepared samples are shown in Figure 5. As seen in Figure 5a, the as-prepared samples exhibit an obvious adsorption edge at about 445 nm, corresponding to a band gap of 2.78 eV. Clearly, the absorption edges of Fw-Co(OH)$_2$/g-C_3N_4 were shifted to a longer-wavelength region than that of pure g-C_3N_4. Moreover, there was an increase in optical absorption in wavelengths ranging from 430 to 750 nm after loading Fw-Co(OH)$_2$ onto g-C_3N_4. This result shows that addition of Fw-Co(OH)$_2$ enhances light-harvesting ability of Fw-Co(OH)$_2$/g-C_3N_4 in the visible-light region. Notably, compared with the edge of g-C_3N_4, the shape of Fw-Co(OH)$_2$/g-C_3N_4 did not alter, indicating that the loading of Fw-Co(OH)$_2$ had no effect on the lattice of g-C_3N_4.

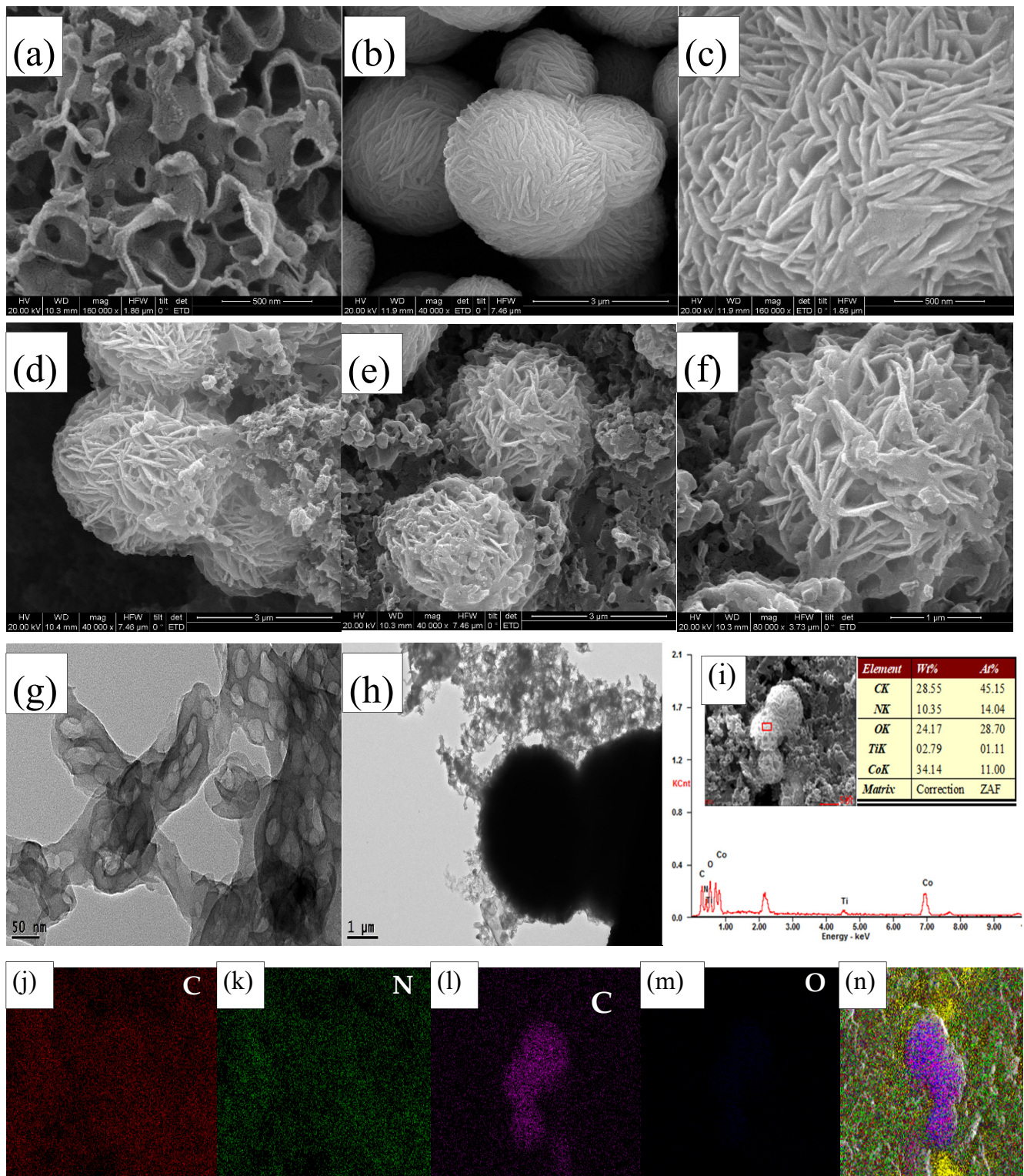**Figure 3.** (**a**) SEM images of g-C$_3$N$_4$, (**b**,**c**) Fw-Co(OH)$_2$, (**d–f**) Fw-Co(OH)$_2$/g-C$_3$N$_4$; (**g**) TEM images of g-C$_3$N$_4$, (**h**) Fw-Co(OH)$_2$/g-C$_3$N$_4$; (**i**) EDX of Fw-Co(OH)$_2$/g-C$_3$N$_4$; (**j–n**) elemental mapping images of a Fw-Co(OH)$_2$/g-C$_3$N$_4$ sample.
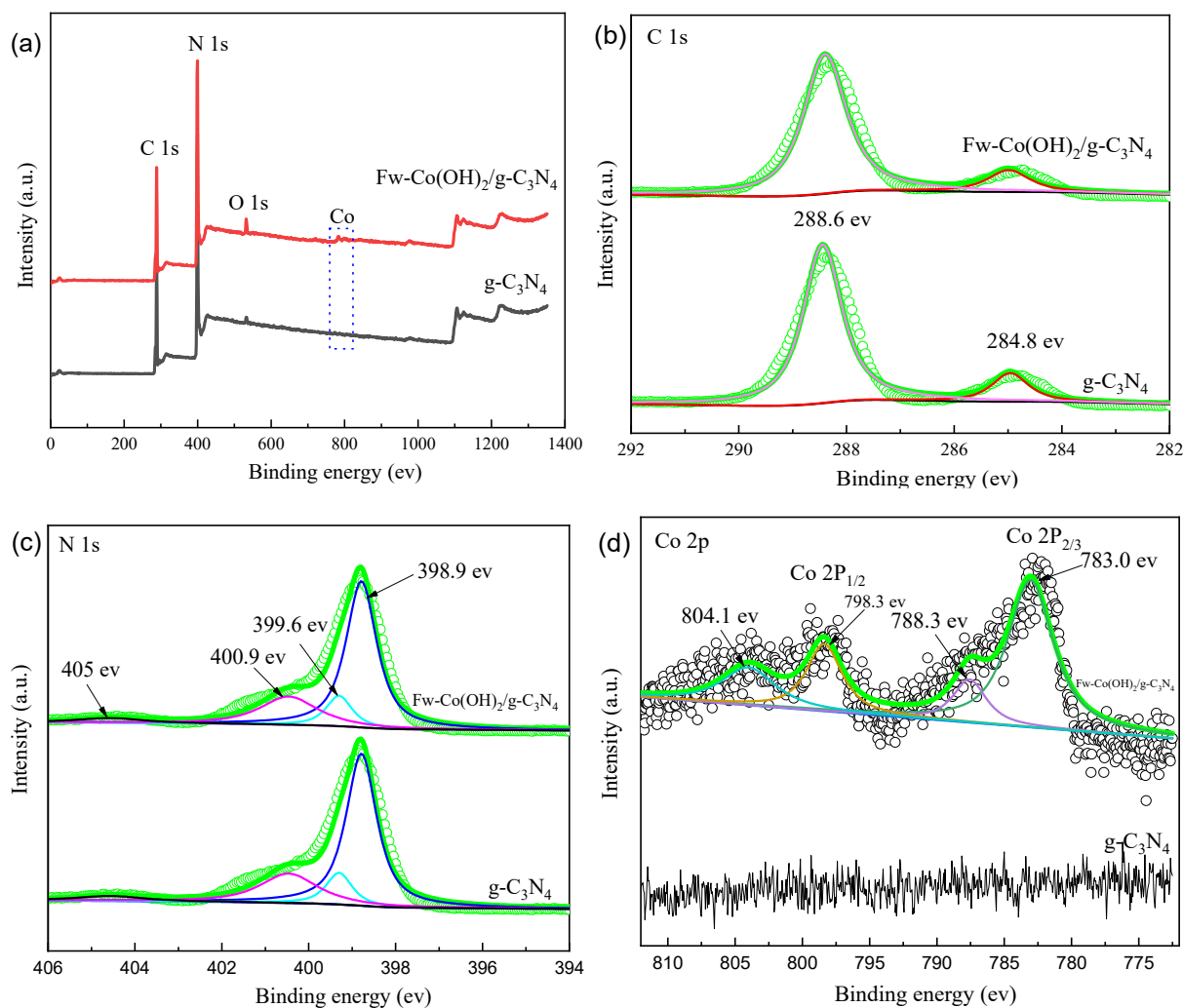
Figure 4. (**a**) XPS survey spectra of g-C_3N_4 and Fw-Co(OH)$_2$/g-C_3N_4; XPS spectra of g-C_3N_4 and Fw-Co(OH)$_2$/g-C_3N_4: (**b**) C 1s; (**c**) N 1s; and (**d**) Co 2p.
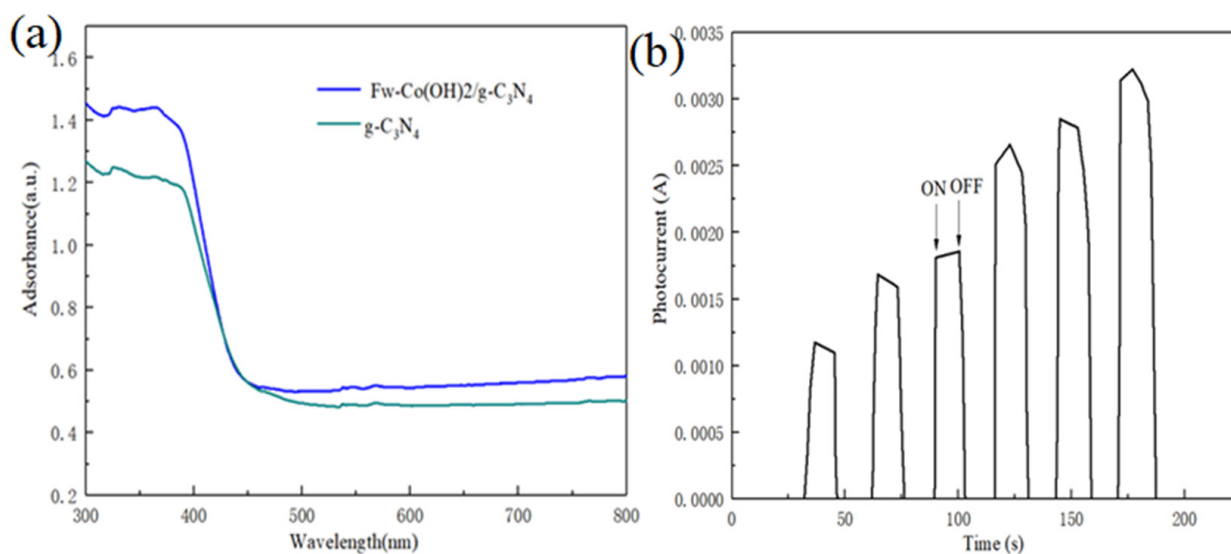
Figure 5. (**a**) UV–vis diffuse reflectance spectra of Fw-Co(OH)$_2$/g-C_3N_4 and g-C_3N_4; (**b**) transient photocurrent responses of the Fw-Co(OH)$_2$/g-C_3N_4 sample in 1M Na$_2$SO$_4$ aqueous solution under visible-light irradiation at 0.5 V vs. Ag/AgCl.

Figure 5b shows the I–t curves for the 25% Fw-Co(OH)$_2$/g-C$_3$N$_4$ with several on-off cycles of intermittent irradiation. As can be seen from this figure's data, the photocurrent value rapidly decreased to zero as soon as the irradiation was turned off, and the photocurrent came back to a constant value when the light was turned on again. This indicates that most of the photogenerated electrons were transported to the back contact across the samples to produce photocurrent under visible-light irradiation.

3.3. Photo(electro)catalytic Degradation of Methylene Blue

In order to optimize the degradation of MB, different ratios of Fw-Co(OH)$_2$ (17, 25 and 50 wt.%) were loaded onto g-C$_3$N$_4$. Figure 6 displayed that, with the weight ratio of Fw-Co(OH)$_2$ increased to 25%, degradation significantly increased also. With a ratio of 25% Fw-Co(OH)$_2$/g-C$_3$N$_4$, degradation can achieve about a 100% ratio within 180 min using visible light, which compared by 17% Fw-Co(OH)$_2$/g-C$_3$N$_4$ that degraded 65% and 50% Fw-Co(OH)$_2$/g-C$_3$N$_4$ that degraded with 80% efficiency. When the weight ratio was further elevated to 50%, the rate dropped by 20%, possibly as a result of extravagant loading of Fw-Co(OH)$_2$ that blocked the optical absorption of g-C$_3$N$_4$. Moreover, MB dye (0.1 moL/L) was degraded by about 32%, 83% and almost 100% for Fw-Co(OH)$_2$, g-C$_3$N$_4$ and Fw-Co(OH)$_2$/g-C$_3$N$_4$ nanocomposites, respectively, after 180 min. It can be easily observed that the Fw-Co(OH)$_2$/g-C$_3$N$_4$ composites showed remarkably enhanced performance compared to pure g-C$_3$N$_4$ and Fw-Co(OH)$_2$. These results suggest that the synergistic and intimate interaction effects between Fw-Co(OH)$_2$ and g-C$_3$N$_4$ are crucial for visible-light catalytic activity. The pseudo-first order equation specified below was applied in order to extract the reaction kinetics of the MB:

$$\ln\left(\frac{C_0}{C}\right) = kt \tag{1}$$

where C is the concentration of the dye at time t, C$_0$ is concentration at time 0 and k is the pseudo-first order rate constant. The plots of ln (C$_0$/C) against irradiation time drawn for all the samples are shown in Figure 6. The degradation rate constants (k) were calculated from the slopes of straight lines drawn using linear regression, according to the first-order kinetic law ln(C$_0$/C) = kt [30,31]. The calculated k values and the corresponding linear regression coefficient degree (R^2) values are shown in Table 1. The values of k and R^2 also clearly indicate that the 25% Fw-Co(OH)$_2$/g-C$_3$N$_4$ preparation exhibits better photocatalytic performance. That is, an appropriate Fw-Co(OH)$_2$ amount promotes photocatalytic activity of g-C$_3$N$_4$ through preventing the recombination of electron-hole pairs. However, abundant loading may possibly hinder the recombination center of photo-generated charge carriers [11].
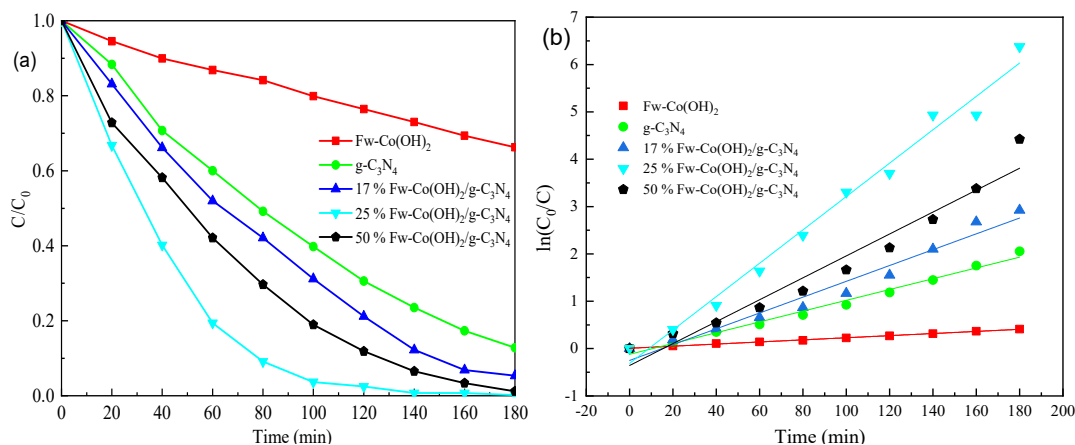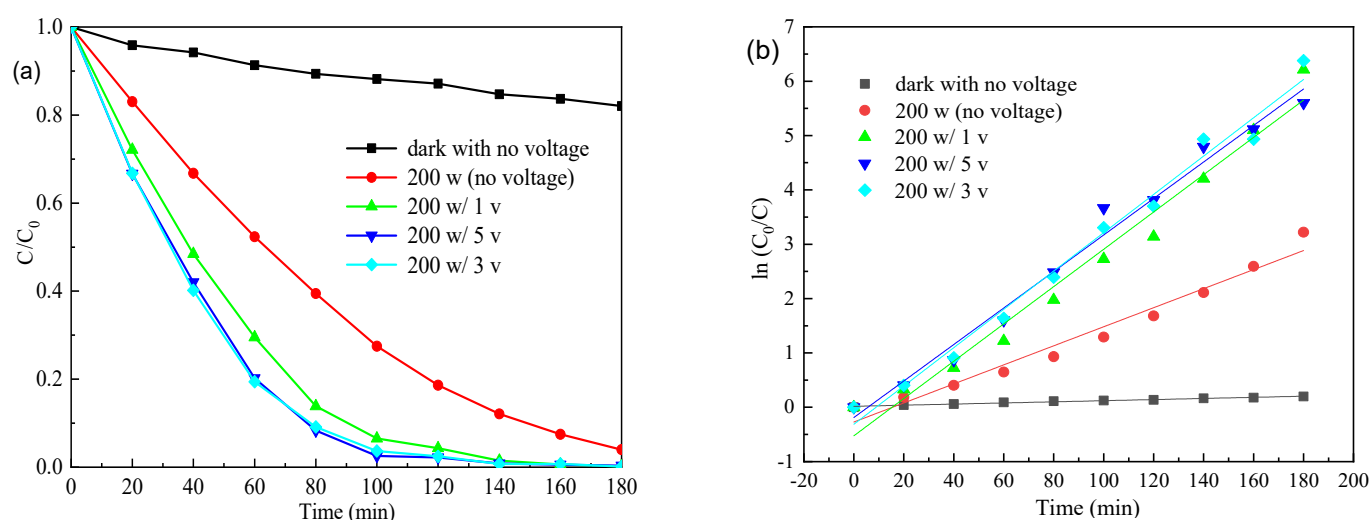

Figure 6. (a) Photo(electro) degradation of MB, (b) linear transform ln (C$_0$/C) of the kinetic curves of MB using different catalysts (light intensity in visible light = 200 W, applied voltage = 200 W).

Table 1. The apparent pseudo-first-order rate parameters of Fw-Co(OH)$_2$/g-C$_3$N$_4$.

Sample	Light Intensity (W)	Voltage (V)	Rate Constant (K), min^{-1}	R^2
Fw-Co(OH)$_2$	200	3	0.0022×10^{-5}	0.9976
g-C$_3$N$_4$	200	3	0.0114×10^{-4}	0.9871
17% Fw-Co(OH)$_2$/g-C$_3$N$_4$	200	3	0.0232	0.9540
25% Fw-Co(OH)$_2$/g-C$_3$N$_4$	200	3	0.0353	0.9856
50% Fw-Co(OH)$_2$/g-C$_3$N$_4$	200	3	0.0167	0.9656
25% Fw-Co(OH)$_2$/g-C$_3$N$_4$	—	—	0.0010×10^{-5}	0.9801
25% Fw-Co(OH)$_2$/g-C$_3$N$_4$	200	—	0.0175	0.9689
25% Fw-Co(OH)$_2$/g-C$_3$N$_4$	200	1	0.0343	0.9736
25% Fw-Co(OH)$_2$/g-C$_3$N$_4$	200	5	0.0336	0.9849
25% Fw-Co(OH)$_2$/g-C$_3$N$_4$	—	3	0.0026×10^{-5}	0.9970
25% Fw-Co(OH)$_2$/g-C$_3$N$_4$	50	3	0.0065×10^{-4}	0.9807
25% Fw-Co(OH)$_2$/g-C$_3$N$_4$	100	3	0.0097×10^{-4}	0.9761

Figures 7 and 8 show the effects of the visible irradiation intensity and applied voltage on the photo (electro) degradation performances of the 25% Fw-Co(OH)$_2$/g-C$_3$N$_4$ in MB solution, respectively. As seen in Figure 7, when the applied voltage increases from 1 V to 5 V, MB removal was only slightly higher. Especially when the voltage changes from 3 V to 5 V, decolorization of MB was achieved to nearly the same extent. The degradation of MB obeyed the pseudo-first-order kinetic model. The apparent rate constants k was summarized in Table 1. The values of MB degradation at different applied voltages had a little difference. As shown in Figure 8, photodegradation of dyes changes with the intensity of light. The k values of MB degradation follow in this order: 200 W > 100 W > 50 W > 0 W (dark). The photocatalytic activity of 25% Fw-Co(OH)$_2$/g-C$_3$N$_4$ drastically increase with increasing light intensity, from 0 W to 200 W. Results reveal that changes in light intensity (50 W to 200 W) play a more important role than the voltage in this system.

Figure 7. (**a**) Photo (electro) degradation of MB, (**b**) linear transform ln (C$_0$/C) of the kinetic curves of MB by 25% Fw-Co(OH)$_2$/g-C$_3$N$_4$ at different voltages.
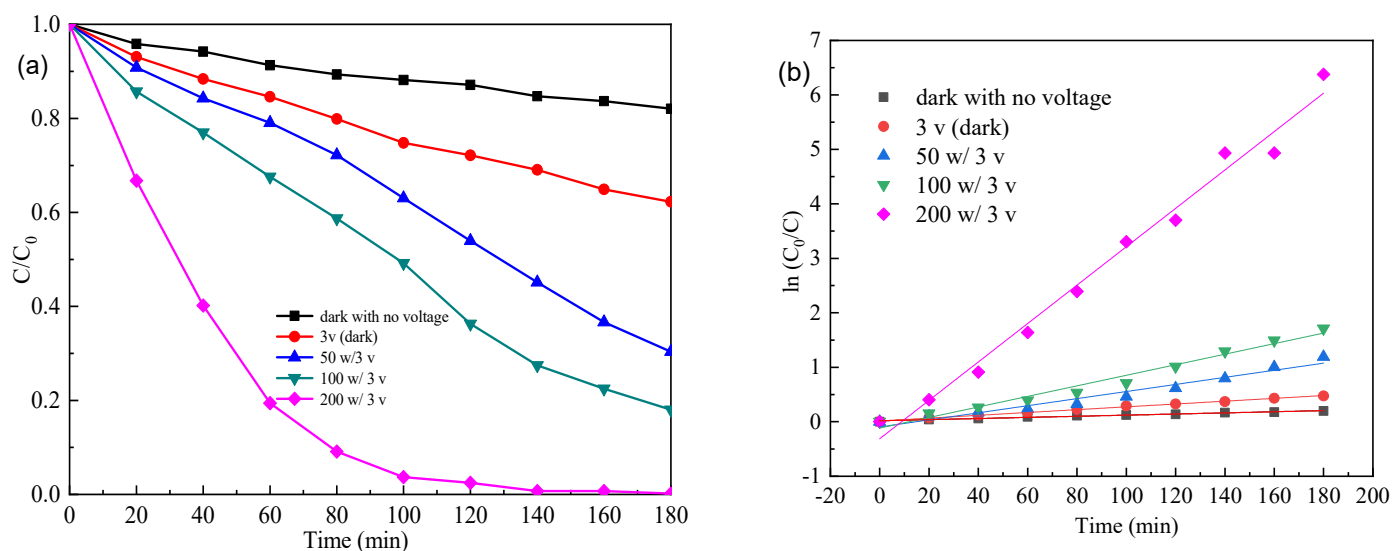
Figure 8. (**a**) Photo (electro) degradation of MB, (**b**) linear transform ln (C_0/C) of the kinetic curves of MB by 25% Fw-Co(OH)$_2$/g-C$_3$N$_4$ at different visible light intensities.

3.4. Photocatalytic Degradation Mechanism

Under visible light irradiation, an electron-hole pair forms, and then a conduction-band electron and a valence-band hole separate on the surface of Fw-Co(OH)$_2$/g-C$_3$N$_4$ (seen in Figure 9). Perhaps the separated hole permits the direct oxidation of MB to reactive intermediates. The increased photocatalytic activity of the coupled photocatalyst was primarily attributed to the enhancements in charge separation efficiency, since a junction was formed by the decoration of Fw-Co(OH)$_2$ with g-C$_3$N$_4$. The PL spectra results also prove that after loading Co(OH)$_2$ NPs onto the surface of g-C$_3$N$_4$, the average lifetimes were significantly increased [32]. Co(OH)$_2$ NP loading remarkably reduced the recombination of carriers, and prolonged the lifetime of photogenerated charge. The junction played an important role in the separation of photogenerated electron-hole pairs. Upon visible excitation, the photogenerated electrons of the Fw-Co(OH)$_2$ conduction band are transferred to the conduction band of g-C$_3$N$_4$. Since the holes move in the opposite direction from the electrons, photogenerated holes become trapped within the Fw-Co(OH)$_2$ particle, causing charge separation to become more efficient. The photogenerated electrons accumulate on the surface of g-C$_3$N$_4$, and can be rapidly transferred to molecular oxygen O$_2$ to form the superoxide radical anion·O$_2{}^-$, which could subsequently generate ·OH radicals and act as effective centers of organic matter mineralization for photocatalytic reactions. The positive holes in the valence band could be trapped by OH$^-$ or H$_2$O species adsorbed on the surface of the catalyst, producing reactive hydroxyl radicals in aqueous media. The active oxygen vacancies that severed as electron acceptors trapped the photoinduced electrons temporarily to restrain the surface recombination of photogenerated electrons and holes. Thus, photocatalytic systems provide broad-range visible light absorption in addition to efficient space separation of photogenerated charge carriers, resulting in efficacious photoactivity. The mechanistic insights infer photocarrier migration and separation, along with the generation of reactive radical species involved in the photodegradation process [11].
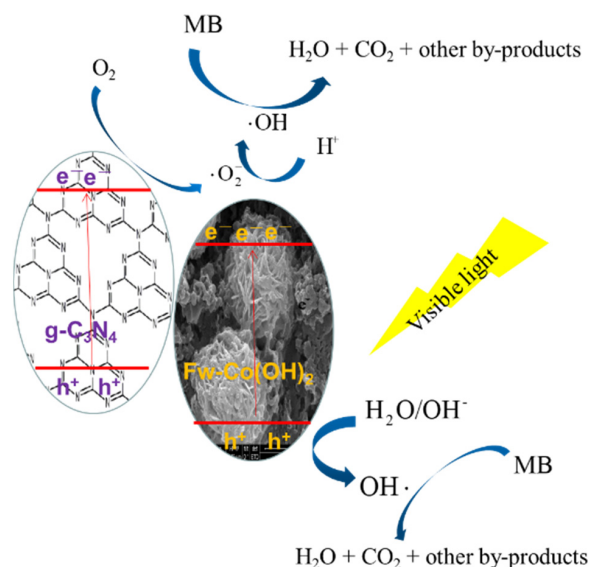
Figure 9. Schematic illustration of a possible mechanism of Fw-Co $(OH)_2$/g-C_3N_4 in MB photocatalytic degradation.

3.5. Stability and Reusability

Practical applicability, stability and recyclability all play an important role in the photocatalytic degradation process. The used Fw-Co$(OH)_2$/g-C_3N_4 catalyst was soaked in deionized water for ten minutes, separated by centrifugation, dried at 60 °C under vacuum and reused. Results in Figure 10 show photocatalytic MB degradation during three consecutive runs with reused photocatalyst. As seen in Figure 10, the stability of 25% Fw-Co$(OH)_2$/g-C_3N_4 catalyst was evaluated; it achieved about 83% and 64% photocatalytic degradation efficiency when the Fw-Co$(OH)_2$/g-C_3N_4 catalyst was reused for the second and third times, respectively. The results show that these materials maintain high MB dye degradation capability after three consecutive cycles under identical conditions, which indicates long-term stability of Fw-Co$(OH)_2$/g-C_3N_4. The decrease in degradation efficiency may be related to the loss of catalyst during the repeated reuse process. Thus, it could be concluded that Fw-Co$(OH)_2$/g-C_3N_4 nanocomposite exhibits good stability and recyclability during the photocatalytic process. This nanocomposite can provide a technical foundation for the use of non-metallic catalysts in dye wastewater treatment.
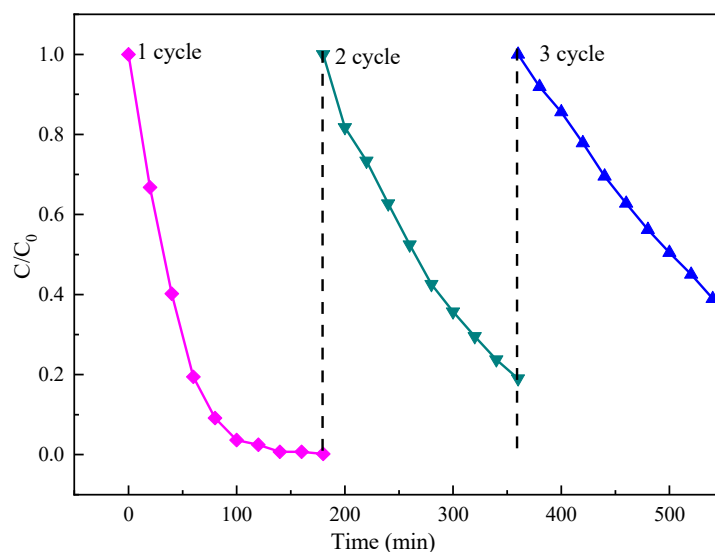

Figure 10. Cyclic photocatalysis of MB under visible light.

4. Conclusions

In summary, Fw-Co(OH)$_2$/g-C$_3$N$_4$ nanocomposite was synthesized via a hydrothermal method for testing enhancement of the photo(electro)catalytic degradation effect. The research results demonstrate that Fw-Co(OH)$_2$/g-C$_3$N$_4$ nanocomposite exhibits better photocatalytic activity as compared to the Fw-Co(OH)$_2$ and g-C$_3$N$_4$ alone, which was mainly attributed to the synergistic effects of interfaces between Co(OH)$_2$ and g-C$_3$N$_4$, and to low recombination of the photogenerated electrons and holes. These nanomaterials were characterized for structure, surface morphology and composition using XRD, SEM and XPS, respectively. The photocatalysts based on g-C$_3$N$_4$ proved their worth by providing extend visible-light absorption, improved space charge separation, along with stimulated migration and enhanced efficacy of various photocatalytic activities, all consistent with previous research [11]. Moreover, the prepared nanocomposite (at the weight ratio of Fw-Co(OH)$_2$ to g-C$_3$N$_4$ equaling 1:3) exhibited excellent photocatalytic response by completely degrading the MB dye at 180 min in a standard three-electrode system. In addition, the Fw-Co(OH)$_2$/g-C$_3$N$_4$ nanocomposite demonstrated that it has good stability for photocatalytic degradation even after three repeated uses. Finally, a suitable photocatalytic reaction mechanism has been proposed to explain the photocatalytic performance of the nanocomposite. The Fw-Co(OH)$_2$/g-C$_3$N$_4$ nanocomposite has superior activity and physico-chemical stability, it can provide a technical foundation for the use of non-metallic catalysts, and has good prospects for becoming widely used in dye wastewater treatment.

Author Contributions: Conceptualization, Q.W.; methodology, Q.L.; validation, Q.L. and Q.W.; formal analysis, Q.L.; resources, Q.W.; data curation, Q.L.; writing—original draft preparation, Q.L.; writing—review and editing, Q.L.; supervision, Q.W.; project administration, Q.W.; funding acquisition, Q.W. All authors have read and agreed to the published version of the manuscript.

Institutional Review Board Statement: Not applicable.

Informed Consent Statement: Not applicable.

Data Availability Statement: All data generated or analyzed during the current study are included in this published article.

Conflicts of Interest: The authors declare no conflict of interest.

References

1. Alqadami, A.A.; Naushad, M.; Alothman, Z.A.; Ahamad, T. Adsorptive performance of MOF nanocomposite for methylene blue and malachite green dyes: Kinetics, isotherm and mechanism. *J. Environ. Manag.* **2018**, *223*, 29–36. [CrossRef] [PubMed]
2. He, Y.; Jiang, D.B.; Chen, J.; Jiang, D.Y.; Zhang, Y.X. Synthesis of MnO$_2$ nanosheets on montmorillonite for oxidative degradation and adsorption of methylene blue. *J. Colloid Interface Sci.* **2018**, *510*, 207–220. [CrossRef]
3. Novais, R.M.; Ascensão, G.; Tobaldi, D.M.; Seabra, M.P.; Labrincha, J.A. Biomass fly ash geopolymer monoliths for effective methylene blue removal from wastewaters. *J. Clean. Prod.* **2018**, *171*, 783–794. [CrossRef]
4. Atchudan, R.; Edison, T.N.J.I.; Perumal, S.; Karthik, N.; Karthikeyan, D.; Shanmugam, M.; Lee, Y.R. Concurrent synthesis of nitrogen-doped carbon dots for cell imaging and ZnO@nitrogen-doped carbon sheets for photocatalytic degradation of methylene blue. *J. Photochem. Photobiol. A Chem.* **2018**, *350*, 75–85. [CrossRef]
5. Dalal, C.; Kumari Garg, A.; Kumar Sonkar, S. Carboxylic Acid-Terminated Carbon Nanoflakes for Selective Adsorption of Water-Soluble Cationic Dyes. *ACS Appl. Nano Mater.* **2021**, *4*, 5611–5620. [CrossRef]
6. Cseri, L.; Topuz, F.; Abdulhamid, M.A.; Alammar, A.; Budd, P.M.; Szekely, G. Electrospun Adsorptive Nanofibrous Membranes from Ion Exchange Polymers to Snare Textile Dyes from Wastewater. *Adv. Mater. Technol.* **2021**, *6*, 2000955. [CrossRef]
7. Yuan, J.; Yi, C.; Jiang, H.; Liu, F.; Cheng, G.J. Direct Ink Writing of Hierarchically Porous Cellulose/Alginate Monolithic Hydrogel as a Highly Effective Adsorbent for Environmental Applications. *ACS Appl. Polym. Mater.* **2021**, *3*, 699–709. [CrossRef]
8. Adeleke, J.T.; Theivasanthi, T.; Thiruppathi, M.; Swaminathan, M.; Akomolafe, T.; Alabi, A.B. Photocatalytic degradation of methylene blue by ZnO/NiFe$_2$O$_4$ nanoparticles. *Appl. Surf. Sci.* **2018**, *455*, 195–200. [CrossRef]

9. Wang, G.H.; Li, Y.J.; Dai, J.L.; Deng, N.S. Highly effcient photocatalytic oxidation of antibiotic ciprofoxacin using TiO_2@g-C_3N_4@biochar composite. *Environ. Sci. Pollut. Res.* **2022**, 1–17. [CrossRef]

10. Ghodsi, S.; Esrafili, A.; Sobhi, H.R.; Rezaei Kalantary, R.; Gholami, M. Synthesis and application of g-C_3N_4/Fe_3O_4/Ag nanocomposite for the effcient photocatalytic inactivation of Escherichia coli and Bacillus subtilis bacteria in aqueous solutions. *AMB Express* **2021**, *11*, 161. [CrossRef]

11. Kumar, A.; Raizada, P.; Singh, P.; Saini, R.V.; Saini, A.K.; Hosseini-Bandegharaei, A. Perspectiveand status of polymeric graphitic carbon nitride based Z-scheme photocatalytic systems for sustainable photocatalytic water purification. *Chem. Eng. J.* **2019**, *391*, 123496. [CrossRef]

12. Fu, J.; Yu, J.; Jiang, C.; Cheng, B. g-C_3N_4/-Based Heterostructured Photocatalysts. *Adv. Energy Mater.* **2018**, *8*, 1701503. [CrossRef]

13. Jiménez-Salcedo, M.; Monge, M.; Tena, M.T. An organometallic approach for the preparation of Au–TiO_2 and Au-g-C_3N_4 nanohybrids: Improving the depletion of paracetamol under visible light. *Photochem. Photobiol. Sci.* **2022**, *21*, 337–347. [CrossRef]

14. Li, W.; Zhang, H.; Chen, W.; Yang, L.; Wu, H.; Mao, N. The effects of cotton cellulose on both energy band gap of g-C_3N_4-TiO_2 nanoparticle sand enhanced photocatalytic properties of cotton-g-C_3N_4–TiO_2 composites. *Cellulose* **2022**, *29*, 193–212. [CrossRef]

15. Razali, M.H.; Md Fauzi, M.A.F.; Mohd Azam, B.; Yusoff, M. g-C_3N_4/TiO_2 nanocomposite photocatalyst for methylene blue photodegradation under visible light. *Appl. Nanosci.* **2022**, *2*, 1–10. [CrossRef]

16. Huo, Y.; Wang, Z.; Zhang, J.; Liang, C.; Dai, K. Ag SPR-promoted 2D porous g-C_3N_4/Ag_2MoO_4 composites for enhanced photocatalytic performance towards methylene blue degradation. *Appl. Surf. Sci.* **2018**, *459*, 271–280. [CrossRef]

17. Liu, M.; Xia, P.; Zhang, L.; Cheng, B.; Yu, J. Enhanced Photocatalytic H2-Production Activity of g-C_3N_4 Nanosheets via Optimal Photodeposition of Pt as Cocatalyst. *ACS Sustain. Chem. Eng.* **2018**, *6*, 10472–10480. [CrossRef]

18. Patnaik, S.; Sahoo, D.P.; Parida, K. An overview on Ag modified g-C_3N_4 based nanostructured materials for energy and environmental applications. *Renew. Sustain. Energy Rev.* **2018**, *82*, 1297–1312. [CrossRef]

19. Feng, J.X.; Ding, L.X.; Ye, S.H.; He, X.J.; Xu, H.; Tong, Y.X.; Li, G.R. Co(OH)$_2$@PANI Hybrid Nanosheets with 3D Networks as High-Performance Electrocatalysts for Hydrogen Evolution Reaction. *Adv. Mater.* **2015**, *27*, 7051–7057. [CrossRef]

20. Zhang, G.; Zang, S.; Wang, X. Layered Co(OH)$_2$ Deposited Polymeric Carbon Nitrides for Photocatalytic Water Oxidation. *ACS Catal.* **2015**, *5*, 941–947. [CrossRef]

21. Nguyen, T.; Boudard, M.; Carmezim, M.J.; Montemor, M.F. Layered Ni(OH)$_2$- Co(OH)$_2$ films prepared by electrodeposition as charge storage electrodes for hybrid supercapacitors. *Sci. Rep.* **2017**, *7*, 39980. [CrossRef]

22. Zhang, H.; Tian, W.; Guo, X.; Zhou, L.; Sun, H.; Tadé, M.O.; Wang, S. Flower-like Cobalt Hydroxide/Oxide on Graphitic Carbon Nitride for Visible-Light-Driven Water Oxidation. *ACS Appl. Mater. Interfaces* **2016**, *8*, 35203–35212. [CrossRef] [PubMed]

23. Huang, Q.; Wang, J.; Liu, F.; Chang, X.; Chen, H.; Lin, H.; Han, S. Graphene-constructed flower-like porous Co(OH)$_2$ with tunable hierarchical morphologies for supercapacitors. *RSC Adv.* **2016**, *6*, 16745–16750. [CrossRef]

24. Lv, H.; Liang, X.; Ji, G.; Zhang, H.; Du, Y. Porous Three-Dimensional Flower-like Co/CoO and Its Excellent Electromagnetic Absorption Properties. *ACS Appl. Mater. Interfaces* **2015**, *7*, 9776–9783. [CrossRef]

25. Zhu, Z.; Huo, P.; Lu, Z.; Yan, Y.; Liu, Z.; Shi, W.; Li, C.; Dong, H. Fabrication of magnetically recoverable photocatalysts using g-C_3N_4 for effective separation of charge carriers through like-Z-scheme mechanism with Fe_3O_4 mediator. *Chem. Eng. J.* **2018**, *331*, 615–625. [CrossRef]

26. Cho, Y.; Lee, J.; Nguyen, T.T.-H.; Bae, J.W.; Yu, T.; Lim, B. Facile synthesis of flower-like α-Co(OH)$_2$ nanostructures for electrochemical water splitting and pseudocapacitor applications. *J. Ind. Eng. Chem.* **2016**, *37*, 175–179. [CrossRef]

27. He, Y.S.; Bai, D.W.; Yang, X.; Chen, J.; Liao, X.-Z.; Ma, Z.-F. A Co(OH)$_2$-graphene nanosheets composite as a high performance anode material for rechargeable lithium batteries. *Electrochem. Commun.* **2010**, *12*, 570–573. [CrossRef]

28. Fang, L.J.; Li, Y.H.; Liu, P.F.; Wang, D.P.; Zeng, H.D.; Wang, X.L.; Yang, H.G. Facile Fabrication of Large-Aspect-Ratio g-C_3N_4 Nanosheets for Enhanced Photocatalytic Hydrogen Evolution. *ACS Sustain. Chem. Eng.* **2017**, *5*, 2039–2043. [CrossRef]

29. Feng, C.; Wang, Z.; Ma, Y.; Zhang, Y.; Wang, L.; Bi, Y. Ultrathin graphitic C_3N_4 nanosheets as highly efficient metal-free cocatalyst for water oxidation. *Appl. Catal. B Environ.* **2017**, *205*, 19–23. [CrossRef]

30. Zhao, J.; Ji, M.; Di, J.; Zhang, Y.; He, M.; Li, H.; Xia, J. Novel Z-scheme heterogeneous photo-Fenton-like g-C_3N_4/FeOCl for the pollutants degradation under visible light irradiation. *J. Photochem. Photobiol. A Chem.* **2020**, *391*, 112343. [CrossRef]

31. Chen, D.; Li, B.; Pu, Q.; Chen, X.; Wen, G.; Li, Z. Preparation of Ag-$AgVO_3$/g-C_3N_4 composite photo-catalyst and degradation characteristics of antibiotics. *J. Hazard. Mater.* **2019**, *373*, 303–312. [CrossRef] [PubMed]

32. Li, Z.; Wu, Y.; Lu, G. Highly efficient hydrogen evolution over Co(OH)$_2$ nanoparticles modified g-C_3N_4 co-sensitized by Eosin Y and Rose Bengal under Visible Light Irradiation. *Appl. Catal. B Environ.* **2016**, *188*, 56–64. [CrossRef]